

Earth and Space Science



RESEARCH ARTICLE

10.1029/2021EA001790

Key Points:

- Noninvasive geophysical characterization of the hyperarid and Mars-like environment of Yungay, Chile using EMI and GPR
- Correlation of ground penetrating radar at the point scale with two open pits located 100 m away from each other
- Upscaling point-scale information using ground penetrating radar and electromagnetic induction to an area of 0.66 hectares (110 x 60 m)

Correspondence to:

A. Klotzsche,
a.klotzsche@fz-juelich.de

Citation:

Dal Bo, I., Klotzsche, A., Bol, R., Moradi, G., Weihermüller, L., Vereecken, H., & van der Kruk, J. (2021). GPR and EMI characterization of the hyperarid study site of Yungay, Chile: Implications of applying geophysical methods on Mars. *Earth and Space Science*, 8, e2021EA001790. <https://doi.org/10.1029/2021EA001790>

Received 8 JUN 2021

Accepted 16 NOV 2021





Author Contributions:

Conceptualization: A. Klotzsche, L. Weihermüller, H. Vereecken, J. Kruk
Formal analysis: I. Dal Bo, G. Moradi, L. Weihermüller, J. Kruk
Funding acquisition: R. Bol, H. Vereecken, J. Kruk
Investigation: I. Dal Bo, G. Moradi, H. Vereecken, J. Kruk
Methodology: I. Dal Bo, A. Klotzsche, G. Moradi, L. Weihermüller, J. Kruk
Project Administration: A. Klotzsche, R. Bol, J. Kruk
Resources: H. Vereecken, J. Kruk

© 2021 The Authors. Earth and Space Science published by Wiley Periodicals LLC on behalf of American Geophysical Union.

This is an open access article under the terms of the [Creative Commons Attribution-NonCommercial-NoDerivs License](#), which permits use and distribution in any medium, provided the original work is properly cited, the use is non-commercial and no modifications or adaptations are made.

GPR and EMI Characterization of the Hyperarid Study Site of Yungay, Chile: Implications of Applying Geophysical Methods on Mars

I. Dal Bo¹, A. Klotzsche¹ , R. Bol¹, G. Moradi¹, L. Weihermüller¹ , H. Vereecken¹ , and J. van der Kruk¹ 

¹Agrosphere (IBG-3), Institute of Bio- and Geosciences, Forschungszentrum Jülich GmbH, Wilhelm-Johnen-Straße, Jülich, Germany

Abstract To unequivocally discover the actual presence of life or even of near surface liquid water on extraterrestrial planetary bodies would be a key scientific breakthrough for humankind. For this reason, studying similar environments on Earth is essential to understanding the processes shaping such extraterrestrial objects. The Yungay area in the Chilean part of the Atacama Desert is deemed to be particularly suitable as a terrestrial analog of Mars (TAM). In this study, we deployed multi-frequency ground penetrating radar (GPR) and a six-coil electromagnetic induction (EMI) system with a maximum depth of investigation of 1.8 m over an area of 0.66 hectares (110 x 60 m). By applying a LOWESS algorithm to the GPR envelope data, we aimed to extrapolate the strongest amplitudes indicating physical contrasts to 3D. The results were constrained with two existing pits 100 m apart. Whereas clay content was mostly responsible for GPR signal attenuation, changes in texture and stratigraphy were linked with strong amplitude reflections. EMI showed very low apparent electrical conductivity (*ECa*) values between 0 and 5 mS/m. The *ECa* variability could be linked to changes in clay content with depth. This agreed with the surface obtained from the LOWESS algorithm. Although soil samples are still necessary to constrain the measured signals, we showed the benefits of applying geophysics for large-scale characterization and can conclude that these two methods are suitable for such hyperarid TAM environments. A similar routine if applied on the surface of Mars could deliver promising results for similar characteristics.

Plain Language Summary Recently, NASA sent the Perseverance rover to Mars (see <https://mars.nasa.gov/mars2020/spacecraft/instruments/>), which is equipped with subsurface radar and other tools to measure surface and subsurface features. The Zhurong Mars rover was also launched by the Chinese government as part of its Tianwen-1 mission (see <https://www.planetary.org/space-missions/tianwen-1>). Such missions apply geophysical methods to noninvasively and indirectly measure the physical properties of the subsurface on a large scale. However, real soil core or profile information is needed to validate the measured signals. In this study, we used ground-penetrating radar and electromagnetic induction to investigate the hyperarid site of Yungay, Atacama, Chile, which is reported to be similar to certain regions of Mars. Our goal was to provide a case study that can be used to calibrate and validate the geophysical data measured on Mars in the near future. We were able to correlate the geophysical data with two excavated pits 100 m away from each other and to upscale this information to an area of 110 x 60 m. As in the case of Yungay, we expect geophysical methods to be primarily influenced by changes in soil particles, compaction, and layering when employed on Mars.

1. Introduction

To unequivocally discover near surface liquid water or the actual presence of life on extraterrestrial planets, as well as understanding their geology and dynamics, would be a huge scientific breakthrough (Arrhenius & Mojzsis, 1996). Most of the current planetary research has been directed toward Mars, mainly due to its similarities and relatively short distance to Earth. Many of these studies have been focused on exploring the atmosphere and the surface of Mars (e.g., Klein, 1979; Holmberg et al., 1980; Glassmeier et al., 2007; Grotzinger et al., 2012; Castaldo et al., 2017). Space missions require significant financial and technical resources, and thus happen on a rather infrequent basis. Therefore, complementary research is undertaken on Earth itself, mainly in Mars-like environments, to improve our understanding of the Red Planet.

Software: I. Dal Bo, A. Klotzsche, J. Kruk

Supervision: A. Klotzsche, R. Bol, L. Weihermüller, H. Vereecken, J. Kruk

Validation: I. Dal Bo, L. Weihermüller

Visualization: I. Dal Bo, J. Kruk

Writing – original draft: I. Dal Bo, A. Klotzsche, R. Bol, L. Weihermüller, H. Vereecken, J. Kruk

Writing – review & editing: A. Klotzsche

Commonly, direct sampling methods such as augering, pit excavation, and rock/soil sampling are used to analyze and understand the distribution of sediments and aggregates, and ultimately to link the results with the climate history (Six et al., 2004; Ewing et al., 2006; Schulze-Makuch et al., 2018). These methods also make it possible to detect the presence of microorganisms (e.g., bacteria) associated with specific subsurface features and/or grain size distribution (Navarro-González et al., 2003; Schulze-Makuch et al., 2018). Despite the conclusive results obtained with such field-based methods, they are restricted to a small sampling volume and are laborious and expensive. Remote sensing techniques, meanwhile, can measure over large areas in a concise time period, but with relatively limited spatial resolution and without the possibility of providing information from the subsurface (Engman, 1991; Lillesand et al., 2014). To bridge the gap between small-scale excavations or augering on one side, and regional-scale measurements from remote sensing on the other side, noninvasive geophysical methods such as ground penetrating radar (GPR) and electromagnetic induction (EMI) have shown significant potential to image the variations in subsurface physical properties in a fast and inexpensive way in a wide range of environments (e.g., Altdorff et al., 2016; De Benedetto et al., 2012; Brogi et al., 2019; Dal Bo et al., 2019). Indeed, linking geophysical signals with processes and stratigraphic variations observed at different depths in the soil pits or with auger information enables a large-scale characterization and paves the way for the use and linkage of remote sensing methods (e.g., Planke et al., 2015; von Hebel et al., 2018). For example, time-domain electromagnetic induction (TDEM) in combination with drilling was successful in detecting standing freshwater in the hyperarid desert of Central Oman due to the presence of clay lenses, which block the downward flow of water (Young et al., 2004). Clay content and, in some cases, the hydraulic conductivity of soils were estimated using GPR and EMI over well-developed desert pavements (Meadows et al., 2006). Due to the low electrical conductivity in dry sandy environments, GPR allows deep signal penetration with the capability of imaging inner structures (e.g., Bristow et al., 2007; Jol & Bristow, 2003).

As many of these studies have shown, geophysical methods have a huge potential to characterize subsurface structures and to bridge the gap between point and remote measurements. The next logical step is to harness this potential for the exploration of extraterrestrial planets. Recent research has focused on applying hydro-geophysical methods to terrestrial analogs of Mars (TAMs) to propose optimal methods for extraterrestrial geophysical exploration (Farr, 2004). It should be noted that most of this research focuses on electromagnetic geophysical methods such as GPR because they are easy to employ in the field and have minimal logistical requirements. For instance, one particular research question centered on the detectability of lava tubes, since these structural elements have been detected by satellite imaging on the surface of Mars and could potentially host living organisms (Léveillé & Datta, 2010). Miyamoto et al. (2005) were able to detect lava tubes at Mount Fuji Volcano in Japan using GPR, with both high spatial resolution and large penetration depth, suggesting the potential for the deployment of GPR to map the same structures on Mars. Similarly, Esmaeili et al. (2020) investigated the potential of GPR to detect and map the geometry of the lava tubes at Lava Beds National Monument in California (USA) and suggested by forward modelling that GPR could be similarly successful on the Moon or Mars. Other studies also focused on applying GPR in terrestrial volcanic environments, proving the suitability of this geophysical method in such settings (Kruse et al., 2010; Courtland et al., 2012; Esmaeili et al., 2017). As significant areas of Mars are covered by ice (e.g., Castaldo et al., 2017; Orosei et al., 2018), Arcone et al. (2002) tested low-frequency GPR systems in Alaska and Antarctica to image the ice and bedrock stratigraphy up to a depth of 80 m, suggesting that these systems could also deliver good results on Mars. Furthermore, the potential presence of brines has been reported on the Red Planet (Zent et al., 1990), which were also highlighted in Antarctica by extensive GPR measurements (Dugan et al., 2015; Forte et al., 2016). Promising GPR results were also obtained by the WISDOM test on the Svalbard islands, where reflectors representing stratigraphic units were imaged down to 6 m depth using a stepped-frequency transmitting antenna with a broad frequency range of 500 MHz to 3 GHz (Ciarletti et al., 2011). Moreover, the integration of autonomous GPR mounted on rovers has been proven to be successful and useful with existing rover technology (Barfoot et al., 2003), with recent tests in the Atacama Desert showing positive results for this application, which could be used on the Red Planet (Gunes-Lasnet et al., 2014).

In the 1970s, GPR was first used during the Apollo 17 mission on the Moon to characterize the surface and interior using frequencies of 5, 15, and 150 MHz (Porcello et al., 1974). Since the beginning of the 21st century especially, we have seen a new push toward the exploration of the Moon. Different expeditions have applied GPR to investigate the lunar surface, thus showing the potential of imaging the shallow regolith (Fang et al., 2014), and have allowed the identification of a complex geological and stratigraphic history along an ~110 m measured transect (Fa et al., 2015; Xiao et al., 2015; Lai et al., 2016). The Chinese Chang'e 3, 4, & 5 missions demonstrated

the ability to obtain detailed images of the stratigraphy and geologic properties of the Moon regolith, as well as the ground properties, showing the possibility of investigating the far side of the Moon (Dong et al., 2021; Leong & Zhu, 2021; Li et al., 2021; Song et al., 2021; Qian et al., 2021; Zhang et al., 2021). In view of the difficulties in retrieving ground truth data in such interplanetary missions, care has to be taken not to interpret ambiguous signal artifacts as real reflections (Li et al., 2018). Given the distance to Mars, the first expeditions only became possible in the last decade, first with orbiting radars and then with surface missions. Orbiting sounding radar has already been deployed on Mars for example by the SHARAD mission (Seu et al., 2007) to image the stratigraphy of the north and south poles (Plaut et al., 2007; Phillips et al., 2008), as well as to distinguish and estimate the dielectric properties of volcanic depositions within sedimentary bodies (Campbell et al., 2008; Carter et al., 2009). Additionally, the possible presence of water bodies has recently been detected at the base of the Martian ice caps using orbiting MARSIS instruments (Orosei et al., 2018). Here, GPR profiles measured between 2012 and 2015 showed relatively high dielectric permittivity (higher than 15), which is compatible with water-bearing materials. The first applications on the surface of Mars have become effective since the year 2020, with measurements and processing still ongoing as of 2021. The Mars 2020 mission has been using the RIMFAX radar system with frequencies ranging between 150 and 1200 MHz mounted to the Perseverance rover, with the main objective of detecting visible layers and assessing the extent and depth of the regolith (Hamran et al., 2015). In the Chinese Mars mission Tianwen-1, started in July 2020, GPR frequencies ranging between 35 and 1800 MHz have been deployed through the Zhurong rover, with a focus on detecting potential ground ice (Zhou et al., 2016; Mallapaty, 2021; Mellon and Sizemore, 2022). Additionally, the WISDOM GPR onboard the Rosalind Franklin rover, which will land on Mars in 2023, is tasked with searching for biological material and is capable of drilling up to 2 m in depth (Ciarletti et al., 2011; Oudart et al., 2021). This system was successfully tested both in dry environments (Atacama Desert and Mount Etna) and in cold environments (glaciers in the Alps) (Ciarletti et al., 2017; Oudart et al., 2021). Finally, possible scenarios of electromagnetic wave propagation and attenuation in the subsurface of Mars have already been studied, taking into account the use of different system frequencies in the presence of electric and magnetic losses as well as heterogeneities within the regolith (Pettinelli et al., 2007; Hamran et al., 2020; Barkataki et al., 2021; Eide et al., 2021).

As all of these successful studies have demonstrated, for low electrical conductivity environments, geophysical methods—and in particular GPR—show great potential for subsurface imaging and have the ability to correlate the obtained physical parameters with both subsurface properties (Dal Bo et al., 2019; De Benedetto et al., 2012) and geochemical indices (Braun et al., 2009). However, difficulties usually arise in obtaining ground truth data in hyperarid and desert environments due to the compactness of the soil (sediments) and bedrock, which makes the interpretation of geophysical data nontrivial (Jol & Bristow, 2003). Therefore, in this paper, we examine the applicability of EMI methods in hyperarid environments as a complementary method as well as their link with GPR data (André et al., 2012). EMI is not often deployed in such settings due to the low electrical conductivity regime, which could potentially lead to unreliable results due to the weak secondary magnetic field generated by the subsurface (e.g., Altdorff et al., 2017). The correlation of depositional patterns and stratigraphy is crucial for the identification of the presence and location of water (past and present). Furthermore, the ability to predict point-scale chemical and physical information is essential to understanding where microbial communities could be located (Navarro-González et al., 2003).

The hyperarid Atacama Desert in Chile is perceived to be a typical Mars-like environment (Navarro-González et al., 2003; Warren-Rhodes et al., 2006; Wettergreen et al., 2005). Within it, the Yungay area near Antofagasta (Figure 1) has been defined as one of the driest places on planet Earth, with an extreme landscape evolution (Hartley & Chong, 2002), climate (less than 2 mm of precipitation per year: Berger & Cooke, 1997; McKay et al., 2003), aggregate distribution (Ewing et al., 2006), and other evidence all pointing to the unsustainability of life (Wierzchos et al., 2006; Wierzchos et al., 2012). However, even in such extreme conditions, traces of life exist and can respond to changes in environmental conditions (Jones et al., 2018; Schulze-Makuch et al., 2018), which suggests the potential of life on other planetary and celestial objects, such as Mars. In particular, the region is a prime example of the type of microbial activity present on the surface of Mars, due to its extreme aridity and long-term climate stability (Wierzchos et al., 2006; Kuhlman et al., 2008). Furthermore, infrared measurements showed how the soil spectra in Yungay are very similar to the bright soil regions on Mars (Preston et al., 2013). The comparability of the analogy between the area of Yungay and the Red Planet can therefore be assumed with regard to the appearance of the soil, the stratigraphy, geology, and the presence of perchlorates. Therefore, an understanding of how soil formation and sediment deposition have evolved in Yungay could be used as a proxy for

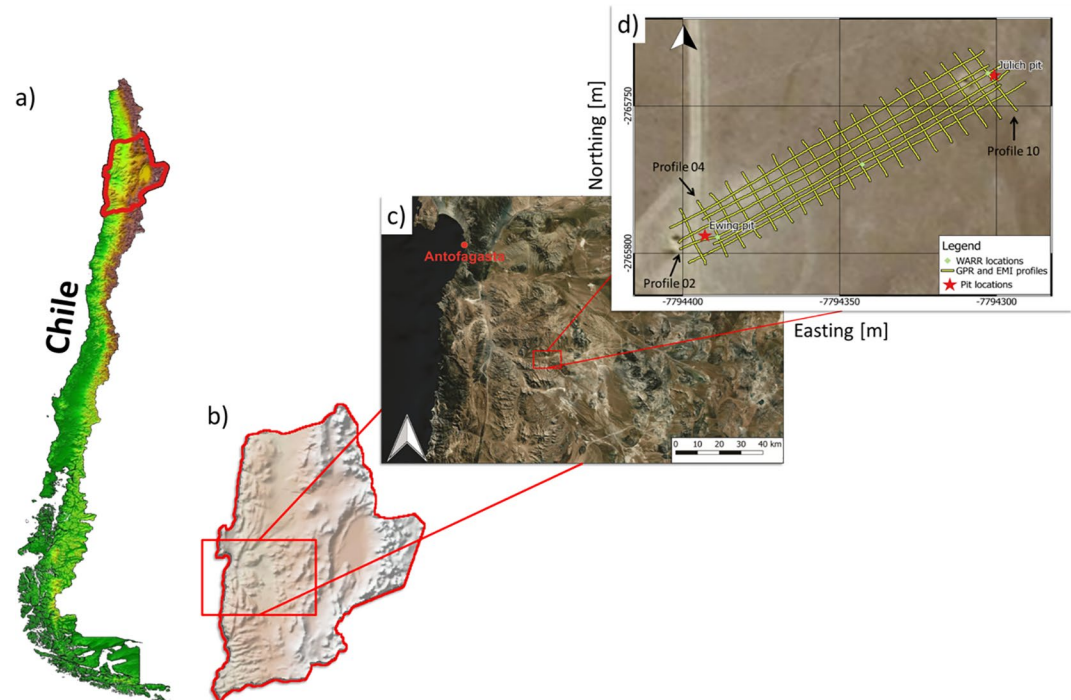


Figure 1. a) Location of the Antofagasta region (Chile) marked in red. b) Study area within the Antofagasta region. c) Antofagasta and surrounding area (Bing Maps ©). d) Details of the study area, where the yellow lines indicate the geophysical profiles.

similar environments on Mars. Specifically for Yungay, Ewing et al. (2006) showed how aggregate distribution with depth is related both to climate variation (i.e., small vs. large precipitation events) and grain size distribution. Ewing et al. (2006) also highlighted the abrupt increment in clay content that could form an impermeable layer for water infiltration, which in turn could influence salt deposition at a certain depth found in the profile. Furthermore, they detected other changes with depth, such as bulk density, caused by compaction and aggregate accumulation.

In this study, we therefore deployed complementary geophysical methods such as GPR and EMI in a TAM context (the hyperarid Atacama Desert). We compared the obtained results with available ground truth data, enabling upscaling from the point scale toward larger local or regional area-based geophysical information, in an effort to shed light on the stratigraphy and geology of the regolith. Specifically, we demonstrated the potential of geophysical methods for hyperarid environments, allowing optimal ground truth sample locations to be defined for detailed point-scale characterization. In particular, we used profile information from the Yungay area published by Ewing et al. (2006) and reported information on depth-related aggregate distribution, extrapolating this point information to a wider area ($\sim 110 \times 60$ m) surrounding the sampling pit. To enable further validation of the geophysical signals, an additional second pit was excavated 100 m away from the Ewing pit and sampled in the framework of the Collaborative Research Project (CRC1211) “Earth – Evolution at the dry limit”.

2. Study Site and Background

2.1. General Study Site Information

The Atacama Desert spans more than 1500 km between the latitudes of 18° S and 28° S, covering 128,000 km² of Chile between the Pacific Ocean and the Andes (Rundel et al., 2007). The yearly average temperature is between 14.5 and 21 °C (Dillon & Hoffmann, 1997), with an average precipitation of less than 2 mm per year (Ewing et al., 2006; Houston & Hartley, 2003). This study focuses on the area of Yungay, Antofagasta (Figure 1). Here, the narrow desert strip located between the Andes on the east and the coastal ridge on the west is known to be one of the driest places on Earth (Amiran & Wilson, 1973; Navarro-González et al., 2003; Ewing et al., 2006).

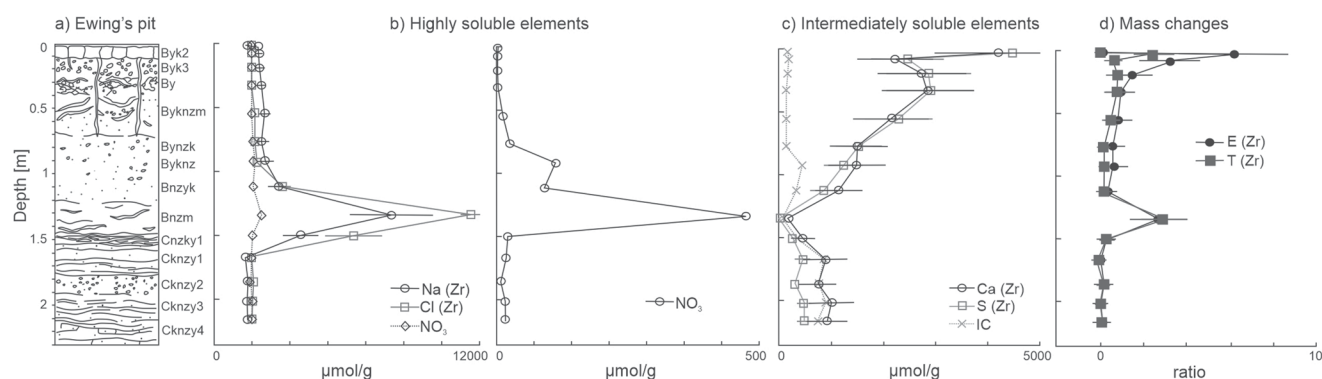


Figure 2. a) Sketch of Ewing's pit (E-pit) with described layers and element distribution. The soil mass and volume change of elements with depth are given for the most soluble elements (b and c), the intermediately soluble salts (d), and finally the total mass (T) and volume (E) changes, using Zr as an immobile element (e). Modified from Ewing et al. (2006).

The evolution of this hyperarid environment in the Atacama is caused by the (dual) rain shadow effect (Houston & Hartley, 2003; Hartley et al., 2005). Moreover, at 1000 m above sea level, a temperature inversion is generated by the cold Humboldt current that limits the inland influence of ocean moisture (Moreno & Gibbons, 2007). All these characteristics severely reduce the amount of precipitation in the central plateaus to such an extreme extent that some locations can be considered to be “Mars-like” (Navarro-González et al., 2003). The soil of the Atacama Desert is known to have the highest nitrate accumulation on Earth and is rich in many other rare minerals (Dunai et al., 2005; Ericksen, 1983). The origin of nitrates and sulfites in the soil has been proven to derive from atmospheric sources (Michalski et al., 2004). Their accumulation over the desert is due to the absence of water denitrification and their limited translocation to deeper zones by percolating water (Dunai et al., 2005; McKay et al., 2003). The study area lies on an alluvial fan surface with a gentle slope ($\sim 1\%$; Ewing et al., 2006) developed between Quaternary and Pliocene (Marinovic et al., 1995; Sernageomin, 1982). The soil surface is steady over time and is mostly composed of sand and small amounts of stones (McKay et al., 2003). Visually, the open pits show an alternation of sand and more clayey layers (Ewing et al., 2006).

2.2. Ewing Pit Profile Description

The Yungay pit excavated by Ewing et al. (2006) was used as one of the two reference locations for our geophysical measurements (see Figures 1d and 2). Briefly, between the surface and a depth of 146 cm, massive sandy and gravelly layers are present with a small percentage of clay at certain depths (15% between 0 and 2 cm and 11% between 26 and 39 cm). Cracks are visible mainly in the upper part up to a depth of 12 cm and from 122 to 146 cm. Beneath this sandy-gravelly facies, the percentage of clay increases to 29% between 146 and 232 cm in depth and thin layers of 1–2 mm thickness are detectable. The bulk density has an average value of 1.0 cm^{-3} in the upper 12 cm, from 1.2 to 1.5 g cm^{-3} between 12 to 102 cm, and below 102 cm the bulk density increases to 1.5 to 1.7 g cm^{-3} . The excavated pit shows that gypsum exceeds anhydrite in the upper 39 cm, whereas below this depth anhydrite exceeds gypsum, which hints that the subsurface is extremely dry. These deposits overlay a zone of halite and nitrate. Sulfates decrease with depth in the upper 122 cm. Chlorides and nitrates increase sharply at 122 cm and below 146 cm only a small amount of salts have accumulated, which is possibly related to the significant increase in clay content below that depth in the profile.

2.3. The Jülich Pit Sampling

Soil samples in the Jülich pit (see location in Figure 1) were taken every 10 cm up to a depth of 120 cm. The fraction above 2 mm (gravel) was separated by sieving. Subsequently, the soil samples were dried for 24 h at a temperature of 105°C . Afterward, the sand fraction between 2 mm and $63 \mu\text{m}$ was determined by wet sieving, and the silt and clay fractions were estimated by the pipette method according to the DIN ISO 11277 standard (determination of particle size distribution by sieving and sedimentation, DIN ISO 11277 (2002)).

3. Geophysical Methods

3.1. Electromagnetic Induction

EMI tools are equipped with at least one coil, which can act as a transmitter (T_x) and receiver (R_{x_n}) alternatively, or with multiple coils, where T_x and R_{x_n} are separated. A primary magnetic field H_p is generated by a current I at a frequency f (which can be fixed or variable) in the kHz range from the transmitting coil. The diffusion of H_p in the subsurface generates an eddy current that triggers a secondary magnetic field, H_s . The ratio between primary and secondary magnetic fields is measured at the receiving coil. This is directly proportional to the ground electrical conductivity σ [mS/m] in the case of a homogeneous half-space layered model (McNeill, 1980; Fitterman, 2015). The measured quantity is a bulk value for a particular depth range depending on the distance s between T_x and R_{x_n} , frequency, and orientation of the coils (horizontal- (HCP) or vertical-coplanar loop (VCP); see McNeill, 1980), which is known as apparent electrical conductivity, ECa .

$$ECa = \frac{4}{\omega s^2 \mu_0} \frac{H_s}{H_p}, \quad (1)$$

where ω is the angular frequency [rad/s] and μ_0 is the magnetic permeability [H/m] of the free space. For the raw EMI data processing, a MATLAB® script was used according to von Hebel et al. (2014) in several steps. First, a histogram filter was applied to the data, which were further filtered for lateral variation of more than 1 mS/m between adjacent points. Finally, a moving average filter was applied and the filtered data were interpolated using an inverse distance weight filter (IDW) in SAGA GIS (Conrad et al., 2015). We chose a grid size of 1.5 m, selecting a quadratic equation for the weights, with a maximum distance of 60 m and a maximum number of 50 points per cell of the grid, which produced a smooth result by filtering the remaining local outliers (Hengl, 2009).

3.2. Ground Penetrating Radar

GPR systems are typically equipped with a transmitting antenna and a receiving antenna. Electromagnetic waves propagate from T_x and a reflected signal is measured by R_x whenever an electromagnetic contrast is present in the physical properties of the subsurface (Annan, 2005; Jol, 2008). There are three main types of GPR: impulse, stepped frequency, and frequency-modulated continuous wave. Here, we focus on impulse GPR systems. The main physical parameters that influence the GPR signal are the relative dielectric permittivity ϵ_r (ratio between the medium dielectric permittivity, ϵ , and the free space dielectric permittivity, ϵ_0) and the electrical conductivity σ [S/m], whereas the magnetic permeability μ [H/m] can often be assumed to be equal to the permeability of the free space, and therefore neglected (Jol, 2008). Dielectric permittivity and electrical conductivity are associated with two key wave field properties, velocity v [m/s] and attenuation α [dB], which can be approximated for high frequencies and for low-loss and non-magnetic media with:

$$v = \frac{c}{\sqrt{\epsilon_r}} \quad (2)$$

and

$$\alpha = \frac{\sigma}{2} \sqrt{\frac{\mu}{\epsilon_r}}, \quad (3)$$

where c is the velocity of light in the free space [m/s]. The transmitted EM wave of impulse GPR systems has a dominant central frequency f_c with a certain bandwidth, while commercial antennae have a range of 20 to 2000 MHz (Jol, 2008). This is directly related to the wavelength of the emitted signal, which can be approximated in free space as $\lambda = v/f$. At higher frequencies, the resolution obtained is higher, whereas the signal penetration is shallower. Therefore, a trade-off between penetration depth and resolution is necessary depending on the environment and on the study goals (Jol, 2008). For surface GPR applications, two types of measurement setup are commonly applied. Common offset profiles (COPs), where the T_x and R_x are moved along the surface with a fixed offset between them, can detect spatial variations of reflectivity and hence subsurface structures. This survey geometry can be applied quickly at field scale to derive structural information. To link the COP to depth, information on the velocity of the medium needs to be known or identified, either by using hyperbolic events in the COP data or by performing point GPR measurements, which are time intensive to measure manually. Such point

measurements are either called common-midpoint (CMP) or wide-angle reflection/refraction (WARR) measurements and collect multiple offset gathers, which allow propagation velocity in the subsurface to be determined. While CMP measurements increase the distance between the Tx and Rx stepwise with a common midpoint, with WARR measurements the Tx is fixed at one location and the distance of the Rx antennae is increased stepwise, resulting in a different midpoint for each measurement. It should be noted that WARR measurements are simpler to collect than CMP gathers, which are in contrast more accurate when dealing with complex subsurface structures.

We performed both GPR measurements using COPs to detect spatial variations and WARR measurements to obtain point-scale velocity distribution at numerous locations. The GPR data were processed using MATLAB®. For COP GPR profiles, a standard routine was applied, including dewow, time-zero correction, a frequency filter, an energy decay recovery function, a median filter, and time-to-depth conversion (Jol, 2008). For the depth conversion, we used the estimated velocity provided from the WARR data. We further calculated instantaneous attributes (envelope, cosine of the phase, and instantaneous frequency) for each COP to enhance the interpretation of the signal (Gross et al., 2003). In particular, we used the instantaneous amplitude (envelope), which gives a quantitative estimate of the subsoil reflectivity independently of the phase (Forte et al., 2012). The calculated analytical signal ($u(t)$) from the measured trace is given by:

$$u(t) = A(t)e^{j\theta(t)}, \quad (4)$$

where $A(t)$ is the envelope and $\theta(t)$ is the instantaneous phase. The WARR data were analyzed using a normalized semblance approach (Heincke et al., 2006; Van der Kruk et al., 2010), which is a very common method for performing a velocity analysis of the signals (for more details, see Dal Bo et al. (2019)). Both linear and hyperbolic moveouts were combined to infer the velocity of the ground wave and reflections, respectively.

In order to extrapolate the strongest amplitudes of the GPR data in 3D, we used the envelope data starting from the GPR COPs in a similar approach to De Benedetto et al. (2012) and André et al. (2012). First, the envelopes of all measured GPR COPs were calculated using Equation (4). The air and ground waves were then muted, and an amplitude threshold was applied to the normalized envelope data. Amplitudes below this threshold were removed. Each point passing the threshold was assigned a set of x , y , and z coordinates, where the latter represents the distance calculated using the average velocity from the WARR data. A surface was then fitted through the 3D cloud of points using a locally weighted nonparametric regression method with a number of points $k = 50$ at each regression step (LOWESS; Cleveland, 1981). The mean square error was used to determine both the ideal number of points k and the final surface. The unsupervised point extraction method is less time consuming and less subjective to errors than handpicking the points in a supervised fashion, although it might only be indicative of where the main dielectric permittivity boundary is located, as the envelope only indicates locations of strong reflectivity, and not the precise onset of the reflection. Therefore, the reliability of the surface obtained needs to be tested. For this reason, the onsets of the high-amplitude reflections were handpicked in each GPR COP to calibrate the defined threshold in the unsupervised method. Pearson's correlation coefficient r was used to determine whether the amplitude threshold was acceptable. By maximizing r , we assumed that no noise was picked up in the unsupervised approach, and hence the extrapolated surface was accepted. Otherwise, the threshold filter was adjusted, and the unsupervised surface was calculated again.

3.3. EMI and GPR Setup

EMI and GPR methods were deployed on a 110 x 60 m (0.66 hectare) grid of inlines (southwest to northeast) and crosslines (southeast to northwest) including the positions where the two pits were excavated (Figure 1). SW to NE profiles were measured every 3.5 m, while the crossing lines (SE to NW) had a spacing of 5 m. In total, 25 profiles were measured with EMI and GPR. For the EMI measurements, the MiniExplorer (GFInstruments, Brno, Czech Republic) equipped with a transmitting coil with a frequency of 30 kHz was used. The instrument has 3 receiver coils at distances of 32, 71, and 118 cm from the transmitter, respectively. The same transects were measured in both HCP and VCP modes, which delivered depths of investigation (DOIs) of 0–1.5 x and 0–0.75 x the distance of the coils, s , respectively. For the GPR measurements, 500 MHz and 1000 MHz pulseEKKO antennae (Sensors & Software Inc, Mississauga, Canada) in COP were used. These antennae emit a pulse with the above-mentioned center frequencies in air. It should be noted that the center frequency of the measured data in the soil is lower than the emitted one. Additionally, WARR measurements were performed at three positions: near the E-pit (Ewing et al., 2006), in the middle of the grid, and near the J-pit (Figure 1). For the 500 MHz

Table 1
Grain Size Distribution of the J-Pit at the Yungay Study Site. Note that the Gravel Content Was Estimated by Sieving (>2mm)

Depth	Clay	Silt	Sand	Gravel
[m]	[%]	[%]	[%]	[%]
0–10	14	13	49	25
10–20	12	13	46	29
20–30	8	14	46	31
30–40	7	14	45	33
40–50	5	35	28	32
50–60	*	*	*	44
60–70	15	14	26	45
70–80	21	21	47	10
80–90	4	12	70	14
90–100	4	10	71	14
100–110	3	8	33	55
110–120	3	8	46	43

Note. * indicates depth intervals for which the fraction size could not be estimated due to flocculation.

measurements, we used a time window of 100 ns, a step size of 5 cm, and a sampling rate of 0.2 ns; while for the 1000 MHz measurements, we used 40 ns, 2 cm, and 0.1 ns, respectively. This enabled us to detect possible lateral variations of velocity, convert time into distance in GPR COPs, and estimate the dielectric permittivity (Equation 2). The geophysical tools were equipped with a high-precision differential GPS (DGPS, with a maximum horizontal precision of 2 cm and a maximum vertical precision of 4 cm, Trimble). The horizontal and vertical precisions reached were 3 and 7 cm, respectively.

4. Results

4.1. Particle Size Depth Distribution in the Jülich Pit (J-Pit)

The J-pit contained between 25 and 55% gravel, except at a depth of between 70 and 100 cm, where only 10–14% gravel was detected. Sand, silt, and clay content were relatively stable up to 40 cm depth with 45–49%, 13–14%, and 7–14%, respectively. Between 40 and 50 cm, the silt content increased to 35% and the sand content decreased to 28%. From 50 to 80 cm, the clay and silt content increased to 21%. The sand content between 80 and 100 cm depth, at ~70%, is the dominant grain size fraction. Clay, silt, and sand all decreased to approximately 4%, 10%, and 40% of the total mass, respectively. An overview of the grain size distribution in the J-pit is provided in Table 1.

The comparison of the grain size distribution between the E-pit (Figure 2) and the J-pit shows lateral changes in grain size and stratigraphy in the investigated 6000-m² area. In the E-pit, the bulk density and gravel content change between the uppermost 100 cm and below. In the J-pit, just 100 m apart, gravel and clay content (and likely also bulk density) change between 50 and 80 cm. These textural differences within the study area might affect the measured geophysical properties, especially as in both cases the clay content increases, whereas the gravel content decreases. Furthermore, the identified interface between the B and C horizons, which appears at different depths in the two pits, could also generate a distinct signal in the geophysical data. At the E-pit, it is described at 146 cm, whereas for the J-pit it was delineated at 90 cm depth.

4.2. EMI and GPR Results

In general, low values of electrical conductivity up to 5.5 mS/m were measured by EMI, which are due to the hyperarid environment (almost absent water content) in the study area. Although this might limit the reliability of EMI measurements, relative *Eca* values can provide qualitative information about the subsurface patterns (Figure 3). Furthermore, the EMI data show an increase in *Eca* with depth of investigation (DOI). Here it should be noted that the first row in Figure 3 shows the EMI measurements in a VCP orientation, while the second row shows the measurements in HCP mode. For each orientation and coil distance, the DOI is also provided in the plots. Therefore, the apparent electrical conductivity measured is influenced more by deeper structures when moving from left to right. As can be seen for the VCP118 (Figure 3c), HCP71 (Figure 3e), and HCP118 (Figure 3f) configurations, a relatively higher conductive area (4 to 5.5 mS/m) is present around the E-pit (Figure 3) compared to the location of the J-pit (1 to 4 mS/m). As the DOI increases from Figure 3a and c, and from d to f, the *Eca* range has more variability for deeper investigation depth and more local heterogeneities will be present (e.g., Figure 3c, e, and f). This is probably due to changes in the subsurface physical properties, both over depth and laterally.

The detected variability in subsurface physical properties also influences the GPR measurements. Figures 4a and 5a show the amplitude variability along a 109-m-long transect (profile 02 in Figure 1) measured with 500 and 1000 MHz GPR COPs from the E-pit to the J-pit. In the radargram, high-amplitude regions are visible for both frequencies at different times (depths) along the profile. High-amplitude reflections (sometimes continuous) in the interval 15 to 25 ns between positions 0 and 25 m (SW) can be detected dipping up and attenuating toward the end of the profile at positions between 80 and 109 m (J-pit). By acquiring WARR measurements at the beginning, middle, and end of profile 02 (Figure 4a, b, and c, respectively), clear reflections could be found at earlier times

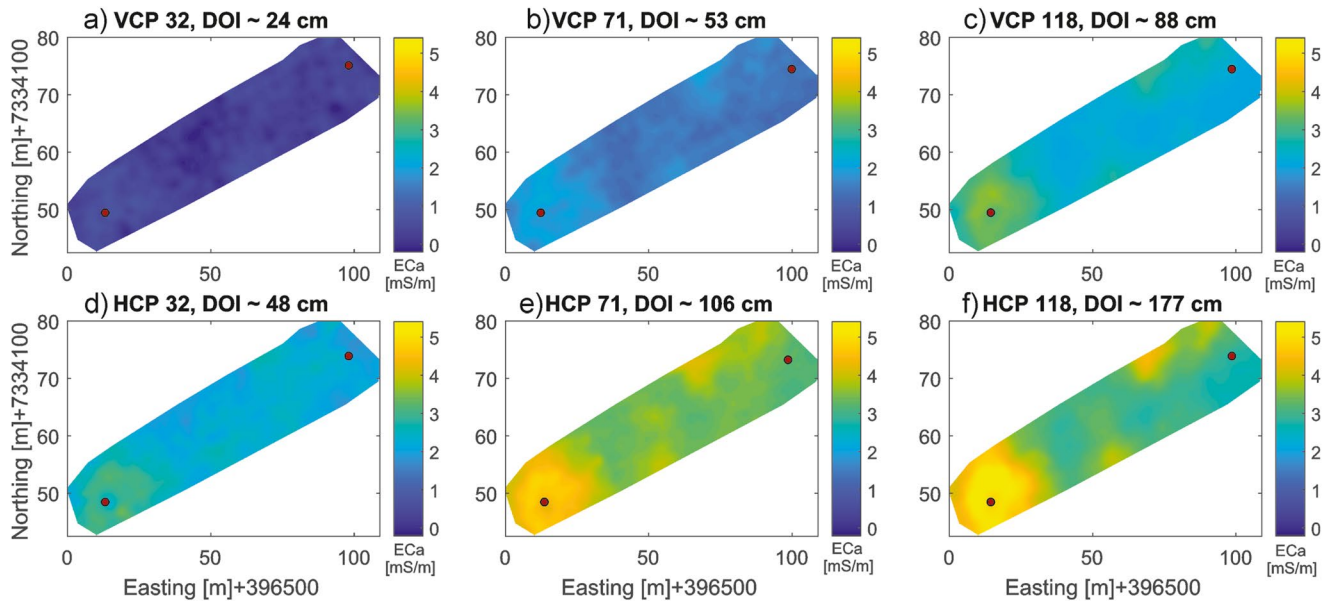


Figure 3. Measured ECa values after inverse distance weight (IDW) interpolation for VCP (a–c) and HCP (d–f) configurations. The DOI is indicated above each plot. The red dots indicate the positions of the E-pit (SW) and the J-pit (NE). The red line indicates profile 02 (Figure 1).

(shallower depths) toward the J-pit, indicating changes in the subsurface physical properties between the two positions. In particular, the upper reflections probably represent the onset of the strong amplitudes visible in the profiles. However, discrepancies between COPs and WARRs arise from the relative position of the transmitter and receiver in the latter measurements, especially when the physical interfaces are not fully horizontal. For this reason, the direction of the WARRs is indicated at the top of Figures 4a and 5a.

The same trend of stronger amplitude attenuation and earlier velocity transition is also visible in the 1000 MHz GPR COPs and WARRs moving from the E-pit to the J-pit (Figure 5). However, while in the 500 MHz GPR data the penetration depth is most likely hampered by global attenuation processes (Jol, 2008) due to the presence of clay in the regolith (Ewing et al., 2006 and Table 1), in the 1000 MHz GPR data the resolution plays a major role in the attenuation, as both ohmic and scattering losses are higher (intrinsic attenuation; see Jol, 2008). The crossline data for the two pit positions (Figures 4e and f, Figures 5e and f) agree with the reflections visible in the inline measurements (Figures 3a and 5a). Especially in profile 04, high-amplitude reflections are present between 15 and 25 ns, which gently dip up from the transect position between 15 and 5 m (Figure 4e). Reflections are also visible in profile 10 (Figure 4f). Here, earlier travel times (at about 10 ns) can be found with weaker amplitudes compared to those of profile 04. Generally, the combination of all the measured COPs shows a common trend with stronger attenuation in the GPR amplitude values toward the northeast part of the area (J-pit) as reflections are found at earlier travel times.

By applying a LOWESS algorithm to the GPR envelope of the 500 MHz (Figure 6a) and 1000 MHz (Figure 6b) measured data, we aimed to extrapolate the high-amplitude signals in 3D. Here, the two pits are indicated with blue (E-pit) and orange (J-pit) dots. In both cases, the depth scale of the surface spans between 70 and 110 cm. Both reflecting layers are deepest in the vicinity of the E-pit, whereas the shallower values were detected at the position of the J-pit. In between the two pits, the reflection layer shows different features between the two frequencies used. The 500 MHz reflection layer (Figure 6a) shows a smooth transition to a peak (at about 40 to 60 m along the east) and a trough (at about 60 to 80 m along the east direction), before dipping up toward the J-pit. On the contrary, the reflection layer calculated from the 1000 MHz data (Figure 6b) shows an abrupt transition to shallower depths (at about 40 cm along the east direction), and the trough is not as evident as for the 500 MHz data (here at about 60 m along the east direction). Generally, the two reflection layers calculated greatly resemble the amplitude variations already visible in the GPR COPs and envelope profiles, with an obtained R^2 and $RMSE$ of 0.23 and 0.16 for the 500 MHz data and 0.21 and 0.17 for the 1000 MHz data.

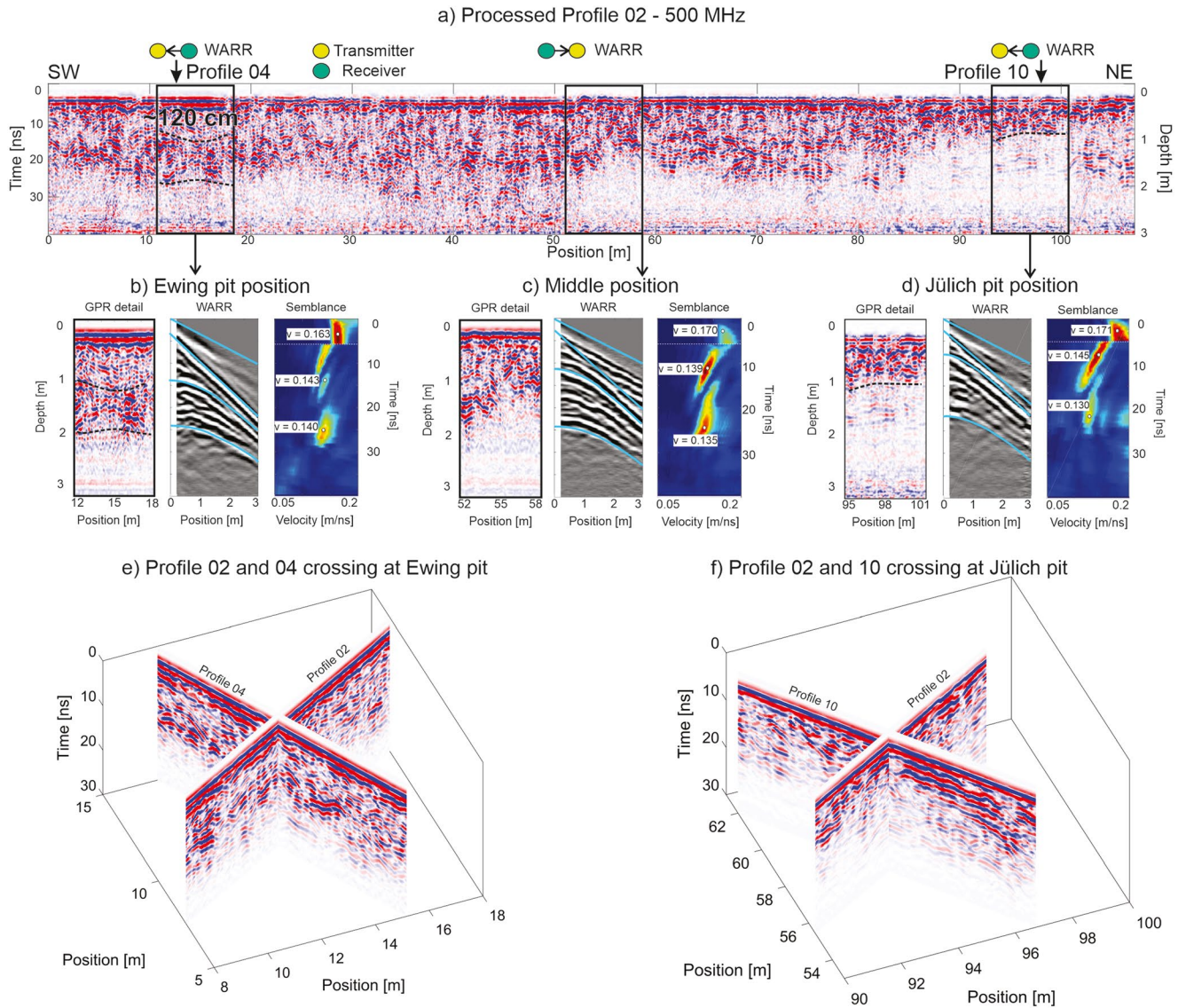


Figure 4. a) GPR COP profile 02 measured with 500 MHz GPR antennae and corresponding WARR measurements at b) the E-pit, c) the middle of the grid, and d) the J-pit. The direction of the WARR measurements is indicated by yellow (transmitter) and green (receiver) dots. Blue lines indicate the picked air wave, ground wave, and reflections visible in the semblance, where the corresponding velocities are indicated. Crossing GPR lines are shown e) at the E-pit and f) at the J-pit, where profile 02 crosses profile 04 and profile 10, respectively (see Figure 1). Note that the air wave has been muted.

5. Discussion

5.1. Comparison Between Geophysical Observations and Ground Truth Data

As shown above, EMI and GPR displayed variability in ECa and amplitude, respectively, in the Yungay area (see Figures 3, 4, and 5). While EMI showed that there are differences in the apparent electrical conductivity within the study site (Figure 3), GPR was able to quantify these differences by analyzing the reflectivity patterns in 3D. In general, changes in horizontal and vertical apparent electrical conductivity were attributed to differences in subsurface clay content between the two pits (E-pit and J-pit, see Figure 2 and Table 1). At the same time, the amount of fine material (especially clay content) is also responsible for the attenuation of the GPR signal (Jol & Bristow, 2003). By comparing Figure 2 (Ewing et al., 2006) and Table 1 with the profiles measured with 500 and 1000 MHz GPR (Figures 4 and 5), it can be clearly seen that the increasing clay content at shallower depth at the J-pit (50 to 70 cm) compared with the E-pit (120 to 146 cm) limits the penetration of electromagnetic waves. On the other hand, the amplitude contrasts in the GPR profiles can be interpreted as being caused by changes in

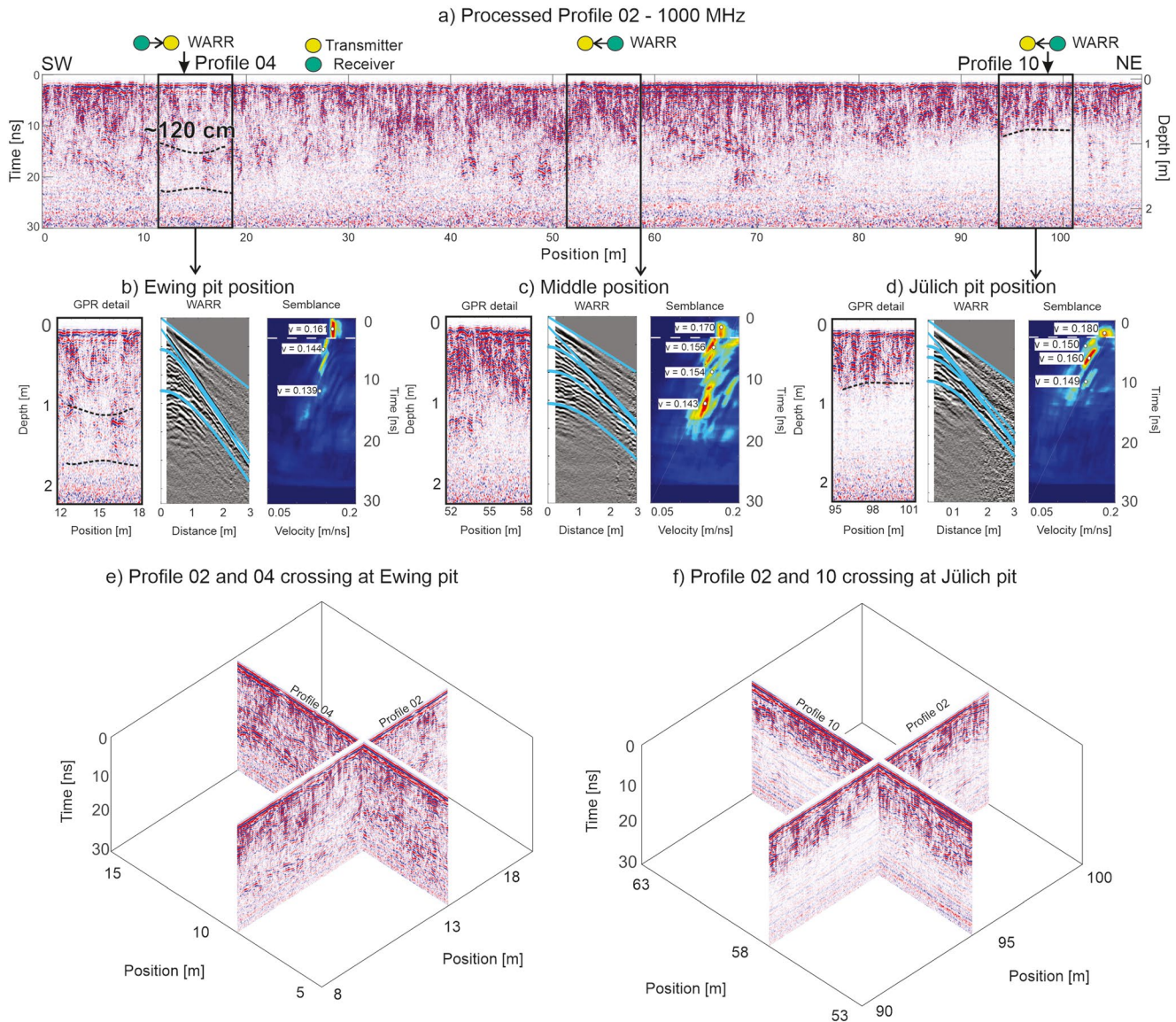


Figure 5. a) GPR COP profile 02 (see Figure 1) measured with 1000 MHz GPR antennae and corresponding WARR measurements at b) the E-pit, c) the middle of the grid, and d) the J-pit. The direction of the WARR measurements is indicated by yellow (transmitter) and green (receiver) dots. Blue lines indicate the picked air wave, ground wave, and reflections visible in the semblance, where the corresponding velocities are indicated. Crossing GPR lines are shown e) at the E-pit and f) at the J-pit where profile 02 crosses profile 04 and profile 10, respectively (see Figure 1). Note that the air wave has been muted.

grain size distribution, bulk density, and layering. To gain a deeper insight into the subsurface from GPR data, we proposed an approach to extrapolate the strong amplitudes measured by applying an LOWESS algorithm to the 500 and 1000 MHz filtered envelope data (Figure 6a and b, respectively; see André et al., 2012; De Benedetto et al., 2012). This resulted in two calculated reflection layers, which were in good agreement with those detectable in the GPR profiles (Figures 4 and 5). However, although the trend obtained mirrors the changes in grain size distribution and stratigraphy obtained from sampling and visible inspection of the pits, the LOWESS interfaces are slightly off the real depth of the layers delineated in the pits. This shift is most likely due to the applied workflow, as the sampled envelope data could differ from the real maxima visible in the GPR profiles. Furthermore, the emitted wavelet is not a pulse but a signal with a specific wavelength (Jol, 2008), and therefore the reflection layers on GPR profiles are visible as intervals of positive and negative amplitude peaks rather than as single points in the time/depth domain (Jol, 2008). This can introduce further uncertainties in linking soil physical properties to geophysical signals. The LOWESS algorithm applied was also used to generate a smooth result in

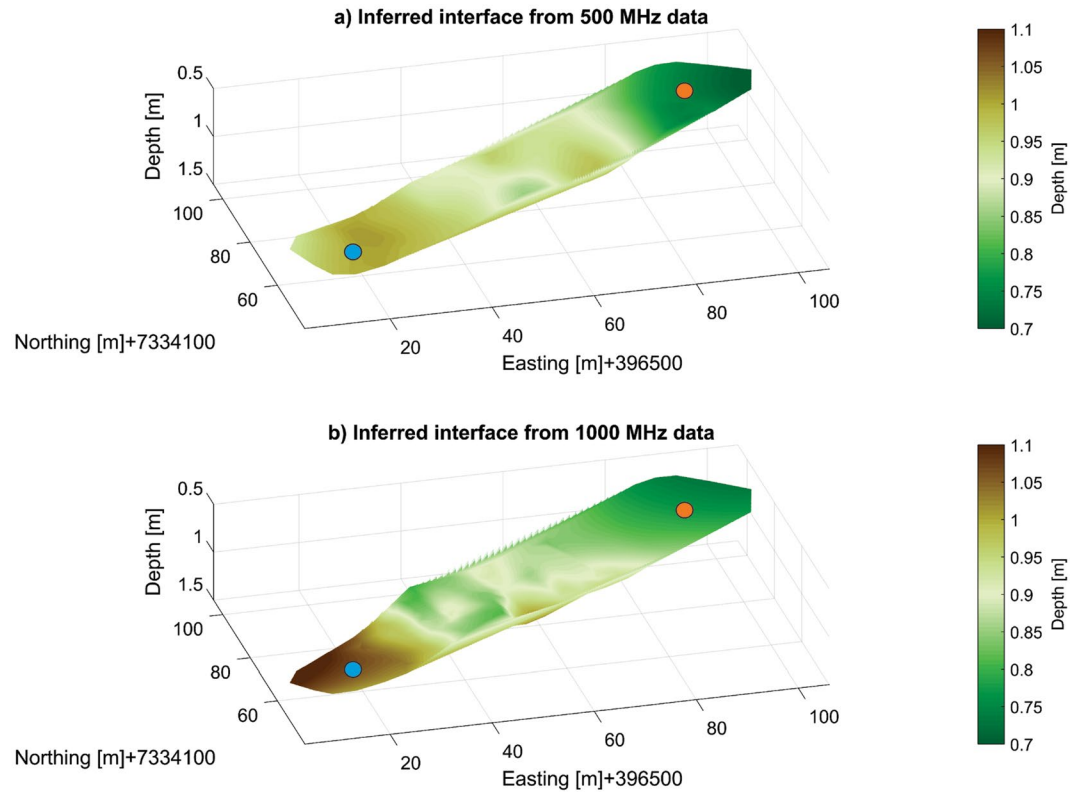


Figure 6. Reflection layer obtained from a) 500 MHz GPR and b) 1000 MHz GPR measurements using an amplitude threshold on the envelope data. The depth spans between 0.7 and 1.1 m for both reflection layers. The two dots indicate the E-pit (blue) and the J-pit (orange).

order to avoid overfitting (Cleveland, 1981). Consequently, the data from the 500 and 1000 MHz measurements along profile 02 (see Figure 1) were interpreted to analyze the differences between the reflections visible in the GPR radargram and the inferred reflection layers derived from the envelope (Figures 7a and b). As stated earlier, the reflection layer from the radargram (black line) and the LOWESS approach (cyan line) show a common trend along profile 02 between the two pits (Figure 7). However, local differences between the two approaches are present, as the interpreted lines (black dashed lines) better resemble the ground truth variability detectable

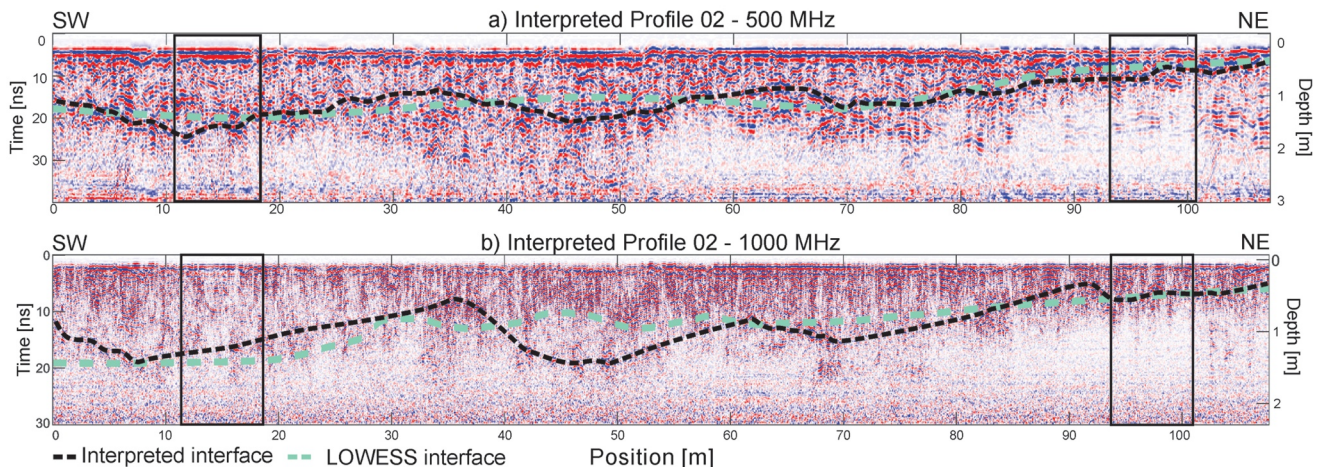


Figure 7. Comparison between interpreted reflection layers (black dashed line) and inferred LOWESS reflection layer (cyan dashed line) in a) 500 MHz and b) 1000 MHz measured GPR data along profile 02 (see Figure 1 for profile location).

Table 2

Correlation Analysis of Geophysical Results. Correlation Analysis of the Obtained Unsupervised GPR Reflection Layer With the Supervised GPR Reflection Layer and EMI Data. The EMI Data Were Correlated Using 3 Coil Offsets for Horizontal and Vertical Orientation. Note That the Nomenclature of the EMI Data Indicates the Depth of Investigation. Strong Correlations Are Highlighted in Bold

Geophysical data	Pearson's statistic of the unsupervised inferred GPR reflection layer	
	500 MHz	1000 MHz
Supervised inferred GPR surface	0.96	0.79
HCP32 ECa data (DOI ~0-48 m)	0.45	0.56
HCP71 ECa data (DOI ~0-106 m)	0.51	0.70
HCP118 ECa data (DOI ~0-177 m)	0.57	0.75
VCP32 ECa data (DOI ~0-24 m)	0.09	0.18
VCP71 ECa data (DOI ~0-53 m)	0.38	0.54
VCP118 ECa data (DOI ~0-88 m)	0.50	0.72

in the two pits. This is mainly true for the 500 MHz measured data, where a good trade-off between resolution and penetration depth can be observed (Figure 7a). On the contrary, the 1000 MHz measured data along the profile (Figure 7) show very detailed features in the upper 50 cm but stronger signal attenuation at greater depth. For example, at the position between 30 and 70 m, there are differences between the two approaches up to 20 and 50 cm depth for both the 500 MHz (Figure 7a) and 1000 MHz (Figure 7b) measured data. Unfortunately, no soil information is available to constrain or verify the visible signals between the two pits. Overall, establishing a link between geophysics and ground truth data at the point scale seems to be fundamental for the interpretation and extrapolation of subsurface features using noninvasive methods as previously stated by Jol and Bristow (2003), Miyamoto et al. (2005), and Meadows et al. (2006). We tested the difference between the reflection layers obtained with the LOWESS algorithm and the interpreted reflection layers picked from the radargram (cyan and black dashed lines, respectively; see Figure 7). In the case of both the 500 and 1000 MHz data, there is a strong correlation between the two methods, as the Pearson's coefficients are 0.96 and 0.79, respectively (Table 2). This indicates that the unsupervised approach is reliable.

5.2. Extrapolation of Soil Data Toward the Large Scale

As shown above, GPR and EMI can provide suitable maps of subsurface variations that can be used to define optimal positions for ground truthing, for example by digging pits or augering (Ciarletti et al., 2011). On the other hand, the classic approach is based on sampling the subsurface randomly or along grid points, which could mean that not all of the range of subsurface properties within the study area will be explored, especially if these features are smaller than the grid spacing of the sampling. Further on, if a link between ground truth data and geophysics is established at the point scale, a large-scale characterization can be performed, as shown by von Hebel et al. (2014). Obtaining soil cores is a crucial point for future missions on Mars that deploy GPR, as similar to Yungay, it might be challenging to obtain ground truth constraints (Hamran et al., 2015; Zhou et al., 2016) despite the fact that drilling devices will be available on the rovers (Ciarletti et al., 2011).

We used GPR and, secondarily, EMI as proxies for ground truth information, attempting to link the geophysical data to variations in grain size and stratigraphy in two excavated pits and to determine whether this information could be extrapolated over the 0.66-ha area measured (De Benedetto et al., 2012). In particular, a surface resembling strong reflection layers was obtained from the 500 and 1000 MHz GPR envelope data by applying a LOWESS algorithm (Cleveland, 1981). As GPR signals could be related to changes in grain size distribution, layering, and bulk density at the two pits, the delineation of the reflection layer will be a fairly good approximation of these property changes in depth. To further constrain the result, we compared the unsupervised delineated reflection layer from the 500 and 1000 MHz measured GPR data with each ECa slice. For deeper depths of investigation (DOIs), the correlation between the specific coil configuration and the reflection layer deduced from the 500 and 1000 MHz GPR data is stronger (Table 2). In particular, for VCP118 (Figure 3c), HCP71 (Figure 3e), and HCP118 (Figure 3f), values of 0.50 and 0.72, 0.51 and 0.70, and 0.57 and 0.75 were obtained for the Pearson's correlation coefficient for the 500 and 1000 MHz reflection layer depth, respectively. Therefore, the ECa values for deeper DOIs in the EMI were more evidently influenced by the differences in subsurface properties generating the reflection layer. One can speculate that the use of larger EMI coil separations and, accordingly, deeper DOIs will result in higher Pearson's correlation coefficients between the reflection layer depth derived from EMI and GPR. This is due to the fact that the changes in soil properties measured at the E-pit and the J-pit would have a stronger impact on the measured ECa due to both coil separation and configuration sensitivity (McNeill, 1980). As we have shown, using geophysics prior to drilling will help to determine the most suitable and interesting locations of changing medium properties, guiding the position for drilling but also minimizing the total number of drills, and therefore helping to save costs and rover resources. Finally, we showed that the use of complementary geophysical methods can help to correlate limited point-scale information from only two pits to the EMI and GPR

signals and to extrapolate the subsurface properties to a larger scale. As a result, this case study could be of help in terms of applying the same methods to future missions studying the subsurface of Mars.

5.3. Application Limitations of Geophysical Methods on Other Planets

GPR has been successfully applied on several planetary missions, both on the Moon and on Mars; however, EMI methods are still an uncharted territory in this regard. Despite showing good results on Earth, there might be several issues with the application of EMI methods on another planet. Firstly, to reach a DOI that allows a good *ECa* estimation, very long and bulky tools need to be deployed. Secondly, as rovers are made of metals, interferences between EMI tools and the rovers themselves might be dominant and not negligible if compared to the signal coming from the subsurface. Lastly, very resistive materials might be present in the shallow soil, similar to what has been seen in Yungay, which would result in very weak generated currents and, in turn, weak secondary magnetic fields (Gromov 1999; Khan et al., 2007; Pettinelli et al., 2007).

Another possible issue with geophysical tools mounted on rovers is the capability of carrying out WARR/CMP measurements. This would require either moving the receiver toward the fixed transmitter or moving both receiver and transmitter toward a middle common point, which seems a daunting job for a rover. For these reasons, the only feasible way of estimating subsurface velocity in this instance is to use scatterers (i.e., hyperbolas visible in GPR profiles); although these are less precise than WARRs/CMPs, they do not require additional measurements (Jacob & Urban, 2015). Another option would be to employ novel approaches based on simultaneous multichannel multi-offset GPR systems (e.g., Kaufmann et al., 2020), which combine the benefits of COP and WARR/CMP acquisition strategies but require more space on a rover.

6. Conclusions

In this study, we used complementary noninvasive, near-surface GPR and EMI measurements in the Atacama Desert, which is known to be an extreme Mars-like environment and proved their suitability for exploring subsurface changes in grain size distribution and stratigraphy. This study confirms the findings of previous measurements in dry environments, where GPR showed enormous potential and enabled extensive imaging of the subsurface. It is well known that the surfaces of the Moon and Mars—depending on the position—have the same characteristics, and therefore it is likely that GPR will continue to be the to-go tool for reconstructing the stratigraphy of other planets. In particular, GPR allowed us to fit a surface to GPR envelope data, which made it possible to infer high-amplitude trends in 3D over the study area. These features were connected at the pit scale to variations in grain size distribution (changes in clay content) and stratigraphy. By comparing the obtained reflection layers from different approaches and with ground truth data, we were also able to prove the reliability of the method. Despite the highly resistive environments, the EMI data showed lateral and vertical *ECa* variations that could be interpreted and linked with the GPR and ground truth data. In particular, increased *ECa* with depth of investigation (DOI) was interpreted as an effect of increasing clay content over depth. This was more evident at the E-pit, where the percentage of clay was higher than that at the J-pit and where the clay-rich layers were found at deeper depths. However, we believe that, where technically possible, EMI should only be used as an auxiliary method. This study showed that GPR and EMI geophysical methods could successfully be applied in a TAM environment, potentially opening up applications on the surface of Mars, where similar conditions could be expected.

Acknowledgments

We acknowledge support from the German Science Foundation's (DFG) priority research program SPP – 1803 “EarthShape: Earth Surface Shaping by Biota” (sub-grants NR 3725/1-1 and SCHA 1690/3-1), DFG project CRC1211 “Earth - Evolution at the Dry Limit”, Terrestrial Environmental Observatories (TERENO), and Advanced Remote Sensing—Ground-Truth Demo and Test Facilities (ACROSS). We would like to thank Maximilian Kanig, Alexis Sepulveda, Theresa Funk, and Cosimo Brogi for their help during fieldwork and in the laboratory.

Data Availability Statement

The data used in this manuscript can be found online (<https://teodoor.icg.kfa-juelich.de/geonetwork/apps/search/?uuid=25786133-f581-4453-8d2b-3066c5c299e0>).

References

- Altdorff, D., Bechtold, M., van der Kruk, J., Vereecken, H., & Huisman, J. A. (2016). Mapping peat layer properties with multi-coil offset electromagnetic induction and laser scanning elevation data. *Geoderma*, 261, 178–189. <https://doi.org/10.1016/j.geoderma.2015.07.015>
- Altdorff, D., von Hebel, C., Borchard, N., van der Kruk, J., Bogena, H. R., Vereecken, H., & Huisman, J. A. (2017). Potential of catchment-wide soil water content prediction using electromagnetic induction in a forest ecosystem. *Environmental Earth Sciences*, 76(3), 111. <https://doi.org/10.1007/s12665-016-6361-3>
- Amiran, D. H., & Wilson, A. W. (1973). *Coastal deserts: Their natural and human environments*. University of Arizona.

- André, F., van Leeuwen, C., Saussez, S., Van Durmen, R., Bogaert, P., Moghadas, D., et al. (2012). High-resolution imaging of a vineyard in south of France using ground-penetrating radar, electromagnetic induction and electrical resistivity tomography. *Journal of Applied Geophysics*, 78, 113–122. <https://doi.org/10.1016/j.jappgeo.2011.08.002>
- Annan, A. P. (2005). In Hydrogeophysics (Ed.), *GPR methods for hydrogeological studies* (pp. 185–213). Springer, edited
- Arcone, S. A., Prentice, M. L., & Delaney, A. J. (2002). Stratigraphic profiling with ground-penetrating radar in permafrost: A review of possible analogs for Mars. *Journal of Geophysical Research: Planets*, 107(E11). <https://doi.org/10.1029/2002je001906>
- Arrhenius, G., & Mojzsis, S. (1996). Extraterrestrial life: Life on Mars—then and now. *Current Biology*, 6(10), 1213–1216. [https://doi.org/10.1016/s0960-9822\(96\)00698-7](https://doi.org/10.1016/s0960-9822(96)00698-7)
- Barfoot, T. D., D'Eleuterio, G. M., & Annan, A. P. (2003). *Proceedings. 2003 IEEE/RSJ International Conference on. Subsurface surveying by a rover equipped with ground-penetrating radar*, paper presented at Intelligent Robots and Systems, 2003.(IROS 2003) IEEE.
- Barkataki, N., Tiru, B., & Sarma, U. (2021). Performance investigation of patch and bow-tie antennas for ground penetrating radar applications, 2021. *International Journal of Advanced Technology and Engineering Exploration*, 8(79), 753–765. <https://doi.org/10.19101/IJATEE.2021.874072>
- Berger, L., & Cooke, R. (1997). The origin and distribution of salts on alluvial fans in the Atacama Desert, northern Chile. *Earth Surface Processes and Landforms*, 22(6), 581–600. [https://doi.org/10.1002/\(sici\)1096-9837\(199706\)22:6<581::aid-esp714>3.0.co;2-4](https://doi.org/10.1002/(sici)1096-9837(199706)22:6<581::aid-esp714>3.0.co;2-4)
- Braun, J.-J., Desclotres, M., Riotte, J., Fleury, S., Barbiéro, L., Boeglin, J.-L., et al. (2009). Regolith mass balance inferred from combined mineralogical, geochemical and geophysical studies: Mule Hole gneissic watershed, South India. *Geochimica et Cosmochimica Acta*, 73(4), 935–961. <https://doi.org/10.1016/j.gca.2008.11.013>
- Bristow, C. S., Duller, G., & Lancaster, N. (2007). Age and dynamics of linear dunes in the Namib Desert. *Geology*, 35(6), 555–558. <https://doi.org/10.1130/g23369a.1>
- Brogi, C., Huisman, J., Pätzold, S., von Hebel, C., Weihermüller, L., Kaufmann, M., et al. (2019). Large-scale soil mapping using multi-configuration EMI and supervised image classification. *Geoderma*, 335, 133–148. <https://doi.org/10.1016/j.geoderma.2018.08.001>
- Campbell, B., Carter, L., Phillips, R., Plaut, J., Putzig, N., Safaeinili, A., et al. (2008). SHARAD radar sounding of the Vastitas Borealis Formation in Amazonis Planitia. *Journal of Geophysical Research: Planets*, 113(E12). <https://doi.org/10.1029/2008je003177>
- Carter, L. M., Campbell, B. A., Holt, J. W., Phillips, R. J., Putzig, N. E., Mattei, S., et al. (2009). Dielectric properties of lava flows west of Ascræus Mons, Mars. *Geophysical Research Letters*, 36(23). <https://doi.org/10.1029/2009gl041234>
- Castaldo, L., Mège, D., Gurgurewicz, J., Orosei, R., & Alberti, G. (2017). Global permittivity mapping of the Martian surface from SHARAD. *Earth and Planetary Science Letters*, 462, 55–65. <https://doi.org/10.1016/j.epsl.2017.01.012>
- Ciarletti, V., Clifford, S., Plettemeier, D., Le Gall, A., Hervé, Y., Dorizon, S., et al. (2017). The WISDOM Radar: Unveiling the Subsurface Beneath the ExoMars Rover and Identifying the Best Locations for Drilling. *Astrobiology*, 17(6-7), 565–584. <https://doi.org/10.1089/ast.2016.1532>
- Ciarletti, V., Corbel, C., Plettemeier, D., Cais, P., Clifford, S. M., & Hamran, S.-E. (2011). WISDOM GPR designed for shallow and high-resolution sounding of the Martian subsurface. *Proceedings of the IEEE*, 99(5), 824–836. <https://doi.org/10.1109/jproc.2010.2100790>
- Cleveland, W. S. (1981). LOWESS: A program for smoothing scatterplots by robust locally weighted regression. *American Statistician*, 35(1), 54. <https://doi.org/10.2307/2683591>
- Conrad, O., Bechtel, B., Bock, M., Dietrich, H., Fischer, E., Gerlitz, L., et al. (2015). System for automated geoscientific analyses (SAGA) v. 2.1.4. *Geoscientific Model Development*, 8(7), 1991–2007. <https://doi.org/10.5194/gmd-8-1991-2015>
- Courtland, L. M., Kruse, S. E., Connor, C. B., Connor, L., Savov, I. P., Martin, K., et al. (2012). GPR investigation of tephra fallout, Cerro Negro volcano, Nicaragua: A method for constraining parameters used in tephra sedimentation models Geophysical imaging of regolith in landscapes along a climate and vegetation gradient in the Chilean coastal cordillera. *Bulletin of volcanology*CATENA, 74180(6), 1409146–1424159.
- Dal Bo, I., Klotzsche, A., Schaller, M., Ehlers, T. A., Kaufmann, M. S., Espoz, J. P. F., et al. (2019). Geophysical imaging of regolith in landscapes along a climate and vegetation gradient in the Chilean coastal cordillera. *CATENA*, 180, 146–159.
- De Benedetto, D., Castrignano, A., Sollitto, D., Modugno, F., Buttafuoco, G., & lo Papa, G. (2012). Integrating geophysical and geostatistical techniques to map the spatial variation of clay. *Geoderma*, 171, 53–63. <https://doi.org/10.1016/j.geoderma.2011.05.005>
- Dillon, M., & Hoffmann, A. (1997). *Lomas formations of the Atacama desert, northern Chile, Centres of plant diversity, a guide and strategy for their conservation* (pp. 528–535).
- DIN, ISO (2002). *Soil quality - Determination of particle size distribution in mineral soil material - Method by sieving and Sedimentation*. (ISO 11277:1998 + ISO 11277:1998 Corrigendum 1:2002) (p. 1127738). <https://doi.org/10.31030/9283499>
- Dong, Z., Fang, G., Zhou, B., Zhao, D., Gao, Y., & Ji, Y. (2021). Properties of lunar regolith on the Moon's farside unveiled by Chang'E-4 Lunar Penetrating Radar. *Journal of Geophysical Research: Planets*, 126, e2020JE006564. <https://doi.org/10.1029/2020JE006564>
- Dugan, H., Doran, P., Wagner, B., Kenig, F., Fritsen, C., Arcone, S., et al. (2015). Stratigraphy of Lake Vida, Antarctica: hydrologic implications of 27 m of ice. *The Cryosphere*, 9(2), 439–450. <https://doi.org/10.5194/tc-9-439-2015>
- Dunai, T. J., López, G. A. G., & Juez-Larré, J. (2005). Oligocene–Miocene age of aridity in the Atacama Desert revealed by exposure dating of erosion-sensitive landforms. *Geology*, 33(4), 321–324. <https://doi.org/10.1130/g21184.1>
- Eide, S., Hamran, S.-E., Dypvik, H., & Amundsen, H. E. F. (2021). Ground-Penetrating Radar Modeling Across the Jezero Crater Floor. *IEEE Journal of Selected Topics in Applied Earth Observations and Remote Sensing*, 14, 2484–2493. <https://doi.org/10.1109/JSTARS.2021.3055944>
- Engman, E. T. (1991). Applications of microwave remote sensing of soil moisture for water resources and agriculture. *Remote Sensing of Environment*, 35(2-3), 213–226. [https://doi.org/10.1016/0034-4257\(91\)90013-v](https://doi.org/10.1016/0034-4257(91)90013-v)
- Ericksen, G. E. (1983). The Chilean Nitrate Deposits: The origin of the Chilean nitrate deposits, which contain a unique group of saline minerals, has provoked lively discussion for more than 100 years. *American Scientist*, 71(4), 366–374.
- Esmaeili, S., Kruse, S., Jazayeri, S., Ewing, S. A., Sutter, B., Owen, J., et al. (2020). Resolution of Lava Tubes with ground penetrating radar: The TubeX projectA threshold in soil formation at Earth's arid-hyperarid transition, *Geochimica et Cosmochimica Acta. Journal of Geophysical Research: Planets*, 12570(21), 5293–5322. e2019JE006138. <https://doi.org/10.1029/2019JE006138>
- Ewing, S. A., Brad, S., Justine, O., Kunihiko, N., Warren, S., Steven, S. C., et al. (2006). A threshold in soil formation at Earth's arid-hyperarid transition. *Geochimica et Cosmochimica Acta*, 70(21), 5293–5322.
- Fa, W., Zhu, M. H., Liu, T., & Plescia, J. B. (2015). Regolith stratigraphy at the Chang'E-3 landing site as seen by lunar penetrating radar. *Geophysical Research Letters*, 42(2310), 179–110. <https://doi.org/10.1002/2015gl066537>
- Fang, G.-Y., Zhou, B., Ji, Y.-C., Zhang, Q.-Y., Shen, S.-X., Li, Y.-X., et al. (2014). Lunar Penetrating Radar onboard the Chang'e-3 mission. *Research in astronomy and astrophysics*, 14(12), 1607, 1622. <https://doi.org/10.1088/1674-4527/14/12/009>
- Farr, T. G. (2004). Terrestrial analogs to Mars: The NRC community decadal report. *Planetary and Space Science*, 52(1), 3–10. <https://doi.org/10.1016/j.pss.2003.08.004>
- Fitterman, D. V. (2015). Tools and Techniques: Active-Source Electromagnetic Methods. Tools and Techniques (pp. 295–333). <https://doi.org/10.1016/b978-0-444-53802-4.00193-7>

- Forte, E., Dalle Fratte, M., Azzaro, M., & Guglielmin, M. (2016). Pressurized brines in continental Antarctica as a possible analogue of Mars. *Scientific reports*, 6, 33158. <https://doi.org/10.1038/srep33158>
- Forte, E., Pipan, M., Casabianca, D., Di Cuia, R., & Riva, A. (2012). Imaging and characterization of a carbonate hydrocarbon reservoir analogue using GPR attributes. *Journal of Applied Geophysics*, 81, 76–87. <https://doi.org/10.1016/j.jappgeo.2011.09.009>
- Glassmeier, K.-H., Boehnhardt, H., Koschny, D., Kührt, E., & Richter, I. (2007). The Rosetta mission: Flying towards the origin of the solar system. *Space Science Reviews*, 128(1–4), 1–21. <https://doi.org/10.1007/s11214-006-9140-8>
- Gromov, V. (1999). Physical and Mechanical Properties of Lunar and Planetary Soils. In P. Ehrenfreund, C. Krafft, H. Kochan, & V. Pirronello (Eds.), *Laboratory Astrophysics and Space Research. Astrophysics and Space Science Library* (Vol. 236.). Springer. https://doi.org/10.1007/978-94-011-4728-6_5. Dordrecht
- Gross, R., Green, A., Horstmeyer, H., Holliger, K., & Baldwin, J. (2003). 3-D georadar images of an active fault: Efficient data acquisition, processing and interpretation strategies. *Subsurface Sensing Technologies and Applications*, 4(1), 19–40. <https://doi.org/10.1023/a:1023059329899>
- Grotzinger, J. P., Crisp, J., Vasavada, A. R., Anderson, R. C., Baker, C. J., Barry, R., et al. (2012). Mars Science Laboratory mission and science investigation. *Space science reviews*, 170(1–4), 5–56. https://doi.org/10.1007/978-1-4614-6339-9_3
- Gunes-Lasnet, S., Kisidi, A., van Winnendael, M., Josset, J., Ciarletti, V., Barnes, D., et al. (2014). SAFER: The promising results of the Mars mission simulation in Atacama, Chile, paper presented at i-SAIRAS 2014: 12th International Symposium on Artificial Intelligence, Robotics and Automation in Space.
- Hamran, S.-E., Berger, T., Brovoll, S., Damsgård, L., Hølleren, Ø., Øyan, M. J., et al. (2015). RIMFAX: A GPR for the Mars 2020 rover mission. paper presented at Advanced Ground Penetrating Radar (IWAGPR), 2015 8th International Workshop on. IEEE.
- Hamran, S. E., Paige, D. A., Amundsen, H. E. F., Berger, T., Brovoll, S., Carter, L., et al. (2020). Radar Imager for Mars' Subsurface Experiment — RIMFAX. *Space Science Reviews*, 216, 128. <https://doi.org/10.1007/s11214-020-00740-4>
- Hartley, A. J., & Chong, G. (2002). Late Pliocene age for the Atacama Desert: implications for the desertification of western South America. *Geology*, 30(1), 43–46. [https://doi.org/10.1130/0091-7613\(2002\)030<0043:lpafat>2.0.co;2](https://doi.org/10.1130/0091-7613(2002)030<0043:lpafat>2.0.co;2)
- Hartley, A. J., Chong, G., Houston, J., & Mather, A. E. (2005). 150 million years of climatic stability: evidence from the Atacama Desert, northern Chile. *Journal of the Geological Society*, 162(3), 421–424. <https://doi.org/10.1144/0016-764904-071>
- Heincke, B., Green, A. G., Van Der Kruk, J., & Willenberg, H. (2006). Semblance-based topographic migration (SBTM): A method for identifying fracture zones in 3D georadar data. *Near Surface Geophysics*, 4(2), 79–88. <https://doi.org/10.3997/1873-0604.2005034>
- Hengl, T. (2009). *A practical guide to geostatistical mapping*. Hengl.
- Holmberg, N. A., Faust, R. P., & Holt, H. M. (1980). *Viking 75 spacecraft design and test summary* (Vol.1). Lander design.
- Houston, J., & Hartley, A. J. (2003). The central Andean west-slope rainshadow and its potential contribution to the origin of hyper-aridity in the Atacama Desert. *International Journal of Climatology*, 23(12), 1453–1464. <https://doi.org/10.1002/joc.938>
- Jacob, R. W., & Urban, T. M. (2016). Ground-Penetrating Radar Velocity Determination and Precision Estimates Using Common-Midpoint (CMP) Collection with Hand-Picking, Semblance Analysis and Cross-Correlation Analysis: A Case Study and Tutorial for Archaeologists. *Archaeometry*, 58, 987–1002. <https://doi.org/10.1111/arc.12214>
- Jol, H. M. (2008). *Ground penetrating radar theory and applications*. Elsevier.
- Jol, H. M., & Bristow, C. S. (2003). GPR in sediments: advice on data collection, basic processing and interpretation, a good practice guide. *Geological Society, London, Special Publications*, 211(1), 9–27. <https://doi.org/10.1144/gsl.sp.2001.211.01.02>
- Jol, H. M., Bristow, C. S., Smith, D. G., Junck, M. B., & Putnam, P. (2003). Stratigraphic imaging of the Navajo Sandstone using ground-penetrating radar. *The Leading Edge*, 22(9), 882–887. <https://doi.org/10.1190/1.1614162>
- Jones, D. L., Olivera-Ardid, S., Klumpp, E., Knief, C., Hill, P. W., Lehndorff, E., & Bol, R. (2018). Moisture activation and carbon use efficiency of soil microbial communities along an aridity gradient in the Atacama Desert. *Soil Biology and Biochemistry*, 117, 68–71. <https://doi.org/10.1016/j.soilbio.2017.10.026>
- Kaufmann, M. S., Klotzsche, A., Vereecken, H., & van der Kruk, J. (2020). Simultaneous multichannel multi-offset ground-penetrating radar measurements for soil characterization. *Vadose Zone J*, 19, e20017. <https://doi.org/10.1002/vzj2.20017>
- Khan, S. D., Heggy, E., & Fernandez, J. (2007). Mapping exposed and buried lava flows using synthetic aperture and ground-penetrating radar in Craters of the Moon lava field. *Geophysics*, 72, B161–B174. <https://doi.org/10.1190/1.2793298>
- Klein, H. P. (1979). The Viking mission and the search for life on Mars. *Reviews of Geophysics*, 17(7), 1655–1662. <https://doi.org/10.1029/rg017i007p01655>
- Kruse, S., Mora-Amador, R., Ramírez, C., & Alvarado, G. E. (2010). *Ground penetrating radar imaging of tephra stratigraphy on Poás and Irazú volcanoes, Costa Rica* (Vol. 43). Revista Geológica de América Central.
- Kuhlman, K. R., Venkat, P., La Duc, M. T., Kuhlman, G. M., & McKay, C. P. (2008). Evidence of a microbial community associated with rock varnish at Yungay, Atacama Desert, Chile. *Journal of Geophysical Research: Biogeosciences*, 113(G4). <https://doi.org/10.1029/2007jg000677>
- Lai, J., Xu, Y., Zhang, X., & Tang, Z. (2016). Structural analysis of lunar subsurface with Chang'E-3 lunar penetrating radar. *Planetary and Space Science*, 120, 96–102. <https://doi.org/10.1016/j.pss.2015.10.014>
- Leong, Z. X., & Zhu, T. (2021). Deep learning lunar penetrating radar inversion: An example from Chang'E-3. *Deep learning lunar penetrating radar inversion: An example from Chang'E-3* (pp. 1379–1383). SEG Technical Program Expanded Abstracts. <https://doi.org/10.1190/segam2021-3581586.1>
- Léveillé, R. J., & Datta, S. (2010). Lava tubes and basaltic caves as astrobiological targets on Earth and Mars: A review. *Planetary and Space Science*, 58(4), 592–598.
- Li, C., Xing, S., Lauro, S. E., Su, Y., Dai, S., Feng, J., et al. (2018). Pitfalls in GPR Data Interpretation: False Reflectors Detected in Lunar Radar Cross Sections by Chang'e-3. *IEEE Transactions on Geoscience and Remote Sensing*, 56(3), 1325–1335. <https://doi.org/10.1109/tgrs.2017.2761881>
- Li, C., Zuo, W., Wen, W., Zeng, X., Gao, X., Liu, Y., et al. (2021). Overview of the Chang'e-4 Mission: Opening the Frontier of Scientific Exploration of the Lunar Far Side. *Space Sci Rev*, 217, 35. <https://doi.org/10.1007/s11214-021-00793-z>
- Lillesand, T., Kiefer, R. W., & Chipman, J. (2014). *Remote sensing and image interpretation*. John Wiley & Sons.
- Mallapaty, S. (2021). What China's mars rover will do next. *Nature*, 593, 323–324. <https://doi.org/10.1038/d41586-021-01301-7>
- Marinovic, S., Smoje, T., Maksae, J., Hervé, A., & Mpodozis, M. (1995). *Hoja aguas blancas*. Región de Antofagasta.
- McKay, C. P., Friedmann, E. I., Gómez-Silva, B., Cáceres-Villanueva, L., Andersen, D. T., & Landheim, R. (2003). Temperature and moisture conditions for life in the extreme arid region of the Atacama Desert: four years of observations including the El Niño of 1997–1998. *Astrobiology*, 3(2), 393–406. <https://doi.org/10.1089/153110703769016460>
- McNeill, J. (1980). *Electromagnetic terrain conductivity measurement at low induction numbers*. Geonics Limited Ontario Canada.
- Meadows, D. G., Young, M. H., & McDonald, E. V. (2006). Estimating the fine soil fraction of desert pavements using ground penetrating radar. *Vadose Zone Journal*, 5(2), 720–730. <https://doi.org/10.2136/vzj2005.0095>

- Mellona, M. T., & Sizemore, H.G. (2022). The history of ground ice at Jezero Crater Mars and other past, present, and future landing sites Author links open overlay panel. *Icarus*, 371, 114667. <https://doi.org/10.1016/j.icarus.2021.114667>
- Michalski, G., Böhlke, J., & Thieme, M. (2004). Long term atmospheric deposition as the source of nitrate and other salts in the Atacama Desert, Chile: New evidence from mass-independent oxygen isotopic compositions. *Geochimica et Cosmochimica Acta*, 68(20), 4023–4038. <https://doi.org/10.1016/j.gca.2004.04.009>
- Miyamoto, H., Haruyama, J. i., Kobayashi, T., Suzuki, K., Okada, T., Nishibori, T., et al. (2005). Mapping the structure and depth of lava tubes using ground penetrating radar. *Geophysical research letters*, 32(21). <https://doi.org/10.1029/2005gl024159>
- Moreno, T., et al. (2007). *The geology of Chile*. Geological Society of London.
- Navarro-González, R., Rainey, F. A., Molina, P., Bagaley, D. R., Hollen, B. J., de la Rosa, J., et al. (2003). Mars-Like Soils in the Atacama Desert, Chile, and the Dry Limit of Microbial Life. *Science*, 302(5647), 1018–1021. <https://doi.org/10.1126/science.1089143>
- Orosei, R., Lauro, S. E., Pettinelli, E., Cicchetti, A., Coradini, M., Cosciotti, B., et al. (2018). Radar evidence of subglacial liquid water on Mars. *Science*, 361(6401), 490–493. <https://doi.org/10.1126/science.aar7268>
- Oudart, N., Ciarletta, V., Le Galla, A., Mastrogioseppe, M., Hervé, Y., Benedix, W.-S., et al. (2021). Range resolution enhancement of WISDOM/ExoMars radar soundings by the Bandwidth Extrapolation technique: Validation and application to field campaign measurements. *Planetary and Space Science*, 197, 105173. <https://doi.org/10.1016/j.pss.2021.105173>
- Pettinelli, E., Burghignoli, P., Pisani, A. R., Ticconi, F., Galli, A., Vannaroni, G., et al. (2007). Electromagnetic Propagation of GPR Signals in Martian Subsurface Scenarios Including Material Losses and Scattering, IEEE Trans. Geosci. Remote Sensing). In *Electromagnetic propagation of GPR signals in Martian subsurface scenarios including material losses and scattering*, IEEE Transactions on Geoscience and Remote Sensing, Mars north polar deposits: Stratigraphy, age, and geodynamical response (Vol. 45, pp. 1271–1281). Science <https://doi.org/10.1109/tgrs.2007.893563>
- Planke, S., Svensen, H., Myklebust, R., Bannister, S., Manton, B., & Lorenz, L. (2015). *Geophysics and remote sensing*.
- Plaut, J. J., Picardi, G., Safaeinili, A., Ivanov, A. B., Milkovich, S. M., Cicchetti, A., et al. (2007). Subsurface radar sounding of the south polar layered deposits of Mars. *Science*, 316(5821), 92–95. <https://doi.org/10.1126/science.1139672>
- Porcello, Grady, L., M., & Barber, S. (1974). The Apollo Lunar Sounder Radar System, Proceedings of the IEEE. Preston. In *TN2: The Catalogue of Planetary Analogues*. ESA.(2013) Milton Keynes, UK.
- Qian, Y., Xiao, L., Wang, q., Head, J. W., Yang, R., Kang, Y., & van der Bogert, C. H. (2021). China's Chang'e-5 landing site: Geology, stratigraphy, and provenance of materials. *Earth and Planetary Science Letters*, 561, 116855. <https://doi.org/10.1016/j.epsl.2021.116855>
- Rundel, P., Villagra, P., Dillon, M., Roig-Juñent, S., & Debandi, G. (2007). *Arid and semi-arid ecosystems* (pp. 158–183). The physical geography of South America.
- Schulze-Makuch, D., Wagner, D., Kounaves, S. P., Mangelsdorf, K., Devine, K. G., de Vera, J.-P., et al. (2018). Transitory microbial habitat in the hyperarid Atacama Desert. *Proceedings of the National Academy of Sciences*, 115(11), 2670–2675. <https://doi.org/10.1073/pnas.1714341115>
- Sernageomin. (1982). *Mapa Geológico de Chile*. Servicio Nacional de Geología y Minería Santiago.
- Seu, R., Phillips, R. J., Biccari, D., Orosei, R., Masdea, A., Picardi, G., & Safaeinili, A. (2007). SHARAD sounding radar on the Mars Reconnaissance Orbiter. *Journal of Geophysical Research: Planets*, 112(E5). <https://doi.org/10.1029/2006je002745>
- Six, J., Bossuyt, H., Degryze, S., & Denef, K. (2004). A history of research on the link between (micro) aggregates, soil biota, and soil organic matter dynamics. *Soil and Tillage Research*, 79(1), 7–31. <https://doi.org/10.1016/j.still.2004.03.008>
- Song, H., Li, C., Zhang, J., Wu, X., Liu, Y., & Zou, Y. (2021). Rock Location and Property Analysis of Lunar Regolith at Chang'E-4 Landing Site Based on Local Correlation and Semblance Analysis. *Remote Sensing*, 13(1), 48. <https://doi.org/10.3390/rs13010048>
- Van der Kruk, J., Jacob, R., & Vereecken, H. (2010). Properties of precipitation-induced multilayer surface waveguides derived from inversion of dispersive TE and TM GPR data. *Geophysics*, 75(4), WA263–WA273. <https://doi.org/10.1190/1.3467444>
- von Hebel, C., Matveeva, M., Verweij, E., Rademski, P., Kaufmann, M. S., Brogi, C., et al. (2018). Understanding soil and plant interaction by combining ground-based quantitative electromagnetic induction and airborne hyperspectral data. *Geophysical Research Letters*, 45(15), 7571–7579. <https://doi.org/10.1029/2018gl078658>
- von Hebel, C., Rudolph, S., Mester, A., Huisman, J. A., Kumbhar, P., Vereecken, H., & van der Kruk, J. (2014). Three-dimensional imaging of subsurface structural patterns using quantitative large-scale multiconfiguration electromagnetic induction data. *Water Resources Research*, 50(3), 2732–2748. <https://doi.org/10.1002/2013wr014864>
- Warren-Rhodes, K. A., Rhodes, K. L., Pointing, S. B., Ewing, S. A., Lacap, D. C., Gómez-Silva, B., et al. (2006). Hypolithic cyanobacteria, dry limit of photosynthesis, and microbial ecology in the hyperarid Atacama Desert. *Microbial Ecology*, 52(3), 389–398. <https://doi.org/10.1007/s00248-006-9055-7>
- Wettergreen, D., Cabrol, N., Baskaran, V., Calderón, F., Heys, S., Jonak, D., et al. (2005). Second experiments in the robotic investigation of life in the Atacama desert of Chile, paper presented at Proc. 8th International Symposium on Artificial Intelligence, Robotics and Automation in Space.
- Wierzchos, J., Ascaso, C., & McKay, C. P. (2006). Endolithic cyanobacteria in halite rocks from the hyperarid core of the Atacama Desert. *Asobiology*, 6(3), 415–422. <https://doi.org/10.1089/ast.2006.6.415>
- Wierzchos, J., de los Ríos, A., & Ascaso, C. (2012). Microorganisms in desert rocks: the edge of life on Earth. *Int Microbiol*, 15, 173–183.
- Xiao, L., Zhu, P., Fang, G., Xiao, Z., Zou, Y., Zhao, J., et al. (2015). A young multilayered terrane of the northern Mare Imbrium revealed by Chang'E-3 mission. *Science*, 347(6227), 1226–1229. <https://doi.org/10.1126/science.1259866>
- Young, M. E., Macumber, P. G., Watts, M. D., & Al-Toqy, N. (2004). Electromagnetic detection of deep freshwater lenses in a hyper-arid limestone terrain. *Journal of Applied Geophysics*, 57(1), 43–61. <https://doi.org/10.1016/j.jappgeo.2004.09.002>
- Zent, A. P., Fanale, F. P., & Roth, L. E. (1990). Possible Martian brines: Radar observations and models. *Journal of Geophysical Research: Solid Earth*, 95(B9), 14531–14542. <https://doi.org/10.1029/jb095ib09p14531>
- Zhang, L., Xu, Y., Bugiolacchi, R., Hu, B., Liu, C., Lai, J., et al. (2021). Rock abundance and evolution of the shallow stratum on Chang'e-4 landing site unveiled by lunar penetrating radar data. *Earth and Planetary Science Letters*, 564, 116912. <https://doi.org/10.1016/j.epsl.2021.116912>
- Zhou, B., Shen, S., Ji, Y., Lu, W., Zhang, F., Fang, G., et al. (2016). The subsurface penetrating radar on the rover of China's Mars 2020 mission. In *International Conference on Ground Penetrating Radar (GPR)*. Paper presented at 2016 16th, IEEE.